Dependence of Atmospheric and Climate Impacts on Launch Latitude and Seasonal Variation in Rocket Emissions

Nattanan Wongprapinkul*[1], Gokcin Cinar†[1], and Oliver Jia-Richards‡[1]

[1]Department of Aerospace Engineering, University of Michigan, Ann Arbor, Michigan, USA

Abstract. Rocket launch emissions, including black carbon (BC), water vapor, and nitrogen oxides, can perturb atmospheric composition and climate, with impacts expected to increase under future growth in launch activity. Previous studies have shown that rocket-emitted BC can warm the stratosphere and alter ozone (O_3), but the dependence of these impacts on launch latitude and seasonal timing remains poorly understood. We investigate how launch latitude and seasonality influence the steady-state distribution of BC and the resulting climate responses. We use the Whole Atmosphere Community Climate Model version 6 to simulate emissions from a medium-lift kerosene launch vehicle at six launch latitudes: 55° S, 29° S, 0° N, 29° N, 55° N, and 70° N. Year-round emissions are applied at all latitudes, while boreal summer-only and boreal winter-only scenarios are applied at selected latitudes using the same annual emission rate, corresponding to 30 Gg yr^{-1} of BC emitted over approximately 11–70 km. The results show that Southern Hemisphere (SH) launches produce larger global BC burdens and stronger stratospheric warming, whereas O_3 depletion is stronger for Northern Hemisphere launches. Launch seasonality modifies BC transport. Low-latitude boreal summer launches transport more BC into the SH, leading to greater stratospheric warming but less O_3 depletion. At higher launch latitudes, launch season controls the altitude of the steady-state BC. These findings indicate that the climate impacts of launch activity depend not only on emission magnitude but also on the latitude and timing of launches.

1 Introduction

Unlike other anthropogenic emissions, which are primarily released in the troposphere and the lower stratosphere, rocket launch emissions are anthropogenic emissions that are directly injected into the stratosphere up to the mesosphere (Brown et al., 2024a). There are several types of rocket propellant systems, four of the most commonly used being solid, cryogenic, hypergolic, and kerosene-based. The major emission products common to these propellant systems include gases such as water vapor (H_2O), carbon dioxide (CO_2), nitrogen oxides (NO_x), and particulates like black carbon (BC) and alumina (Dallas et al., 2020).

In terms of the environmental impacts, stratospheric temperature changes are influenced by multiple factors associated with rocket emissions. BC absorbs both incoming shortwave radiation from the sun and reflected shortwave radiation from the surface and atmosphere, thereby heating the surrounding air (Ross et al., 2010; Yu et al., 2019; Maloney et al., 2022). In contrast,

*Doctoral Candidate, Department of Aerospace Engineering, nattanan@umich.edu

†Assistant Professor, Department of Aerospace Engineering, cinar@umich.edu

‡Assistant Professor, Department of Aerospace Engineering, oliverjr@umich.edu

an increase in stratospheric H_2O enhances the stratosphere's ability to emit infrared radiation to space, potentially leading to cooling (Kirk-Davidoff et al., 1999; Randel et al., 2004; Tian et al., 2009; Larson et al., 2017; Charlesworth et al., 2023). NO_x contributes indirectly to temperature changes by modifying ozone (O_3) concentrations, which affects the radiative balance and influences stratospheric temperatures. The alterations in stratospheric temperature can further influence the general circulation. One example is Sudden Stratospheric Warming (SSW), which can alter the surrounding temperatures and potentially inter-hemispheric temperatures through gravity waves and planetary-wave forcing (Baldwin et al., 2021; Eswaraiah et al., 2022; Okui et al., 2025).

In terms of O_3 depletion, stratospheric BC and NO_x emissions have been found to have significantly greater impacts compared to other emission products (Larson et al., 2017; Tsigaridis et al., 2024). BC depletes O_3 by altering the stratospheric temperature, which accelerates O_3-destroying chemical cycles and affects atmospheric transport processes (Ross et al., 2010; Revell et al., 2025). NO_x activates the catalytic O_3 destruction cycle and is considered the single most important O_3-depleting emission (Crutzen, 1970; Ravishankara et al., 2009). H_2O in the upper stratosphere can photolyze to form hydrogen oxides (HO_x), which in turn catalyze O_3 depletion (Brown et al., 2024a). Moreover, changes in stratospheric H_2O content can influence the formation of Polar Stratospheric Clouds (PSCs), which enhance chemical reactions that lead to O_3 depletion (Tian et al., 2009; Vogel et al., 2011; Rosenlof, 2018). However, stratospheric cooling resulting from increased H_2O can lead to an increase in O_3 (Larson et al., 2017; Rosenlof, 2018).

Most studies about the atmospheric impact of rocket emissions considered radiative forcing (RF) as one of the primary responses (Ross et al., 2010; Ross and Sheaffer, 2014; Larson et al., 2017; Ross, 2020; Ryan et al., 2022; Maloney et al., 2022). Two types of RF are usually considered. Instantaneous radiative forcing (IRF) evaluates the immediate perturbation of the Earth's energy balance. Unlike IRF, effective radiative forcing (ERF) accounts for rapid adjustments in the atmosphere, including shifts in atmospheric temperature profiles, while maintaining fixed sea surface temperatures (SSTs), which makes it a better indicator of aerosol-induced global mean temperature response (Myhre et al., 2014).

This study builds upon previous work investigating the climate impacts of projected future space launch rates, which has shown that rocket emissions can perturb the climate through increases in stratospheric temperature, O_3 depletion, and changes in Earth's radiative balance, highlighting the critical role of BC emissions (Ross et al., 2010; Maloney et al., 2022; Tsigaridis et al., 2024; Revell et al., 2025). These studies, however, typically assume a single launch location or a globally uniform launch distribution, as well as continuous, steady launch emissions, thereby limiting insight into how geographic and seasonal variability in launch activity may modulate atmospheric transport and climate responses. As a result, the dependence of long-term stratospheric and climate impacts on launch latitude and seasonality remains poorly explored. Given the uneven global distribution of launch sites and the ongoing expansion of launch infrastructure into new geographic regions and latitude bands driven by increasing commercial and governmental launch demand (Jones et al., 2025), understanding the latitudinal dependence of rocket emissions is important for assessing long-term climate impacts. Moreover, interplanetary missions are constrained by relatively narrow launch windows determined by orbital alignment (ESA, 2002), raising the question of whether launch timing could systematically influence long-term climate effects. This study addresses these gaps by examining how variations in launch latitude and seasonal timing influence the spatial profile and magnitude of climate responses. The hypothesis is that if

the location and seasonal timing of rocket launches vary, then the resulting distribution and transport of BC in the stratosphere will differ, leading to distinct long-term regional and global climate impacts.

To test this hypothesis, this study investigates the latitudinal and seasonal dependencies of atmospheric impacts of a medium-lift kerosene launch vehicle, focusing on the key emitted species (BC, NO_x, and H_2O). Each case simulates 20 years of launches using the Whole Atmosphere Community Climate Model version 6 (WACCM6) with a consistent annual launch frequency, corresponding to a BC emission rate of 30 Gg yr^{-1} integrated over model layers corresponding to geometric altitudes of approximately 11–70 km, which is comparable to a recent Australian wildfire event that released approximately 22.5 Gg of BC into the stratosphere (Yu et al., 2021). The ambitious future launch-growth scenario estimated by Revell et al. (2025) projects approximately 2×10^3 launches per year by 2030, corresponding to roughly 4.25 Gg yr^{-1} of BC emissions into the atmosphere, which is approximately one-seventh of the BC emission rate adopted in this study. This emission rate of 30 Gg yr^{-1}, shown by Maloney et al. (2022) to produce statistically significant climate impacts, is hypothetical and is used solely for comparison of long-term underlying climate impacts among the experimental cases. To assess latitudinal dependencies, launches are simulated from six latitudes (55° S, 29° S, 0° N, 29° N, 55° N, and 70° N). To examine seasonal dependencies, boreal summer-only and boreal winter-only cases are performed. An additional BC-only case at 29° N is included to help isolate the role of BC in long-term climate impacts compared to NO_x and H_2O. A control simulation without rocket emissions is also conducted for comparison with the launch cases. The analysis quantifies long-term responses in stratospheric temperature, O_3 concentration, and ERF. This approach enables a detailed comparison of the resulting atmospheric outcomes and clarifies the cause-effect mechanisms driving these climate responses, highlighting the significance of launch latitude and seasonality in shaping atmospheric impacts.

2 Methods

This study uses WACCM6 with the year-2000 fixed SST configuration to simulate medium-lift kerosene rocket emissions, including BC, NO_x, and H_2O. Emissions were derived from trajectory data and emission indices. Details regarding the climate model and experiment design are provided below. Simulations were conducted for six launch latitudes, including boreal summer-only and boreal winter-only scenarios at four latitudes. A control simulation without rocket emissions and an additional BC-only case at 29° N were also included.

2.1 Climate Model

This study uses WACCM6 (Gettelman et al., 2019), which is part of the Community Earth System Model version 2 (CESM2) framework (Danabasoglu et al., 2020). WACCM6 has several improvements over WACCM4, enhancing the representation of atmospheric and climate processes (Gettelman et al., 2019). The model uses the Community Atmosphere Model version 6 (CAM6) physics, with a focus on middle atmospheric processes and a reduced set of tropospheric chemical reactions, which offer lower computational cost. Climatological forcings were applied with fixed SSTs, representing conditions from the year 2000, consistent with Ross et al. (2010) and selected cases in Maloney et al. (2022). As noted by Maloney et al. (2022), us-

ing fixed SSTs reduces internal variability, allowing the stratospheric response to BC emissions to be more clearly identified. This approach also enables a more precise estimation of the ERF, making it particularly suitable for studies focused on stratospheric processes. The model includes 70 vertical levels, extending from the surface up to approximately 140 km altitude. The horizontal grid resolution is set to 1.9° latitude×2.5° longitude. The BC properties are specified as a diameter of 0.134 μm and a density of 1,700 kg m^{-3}, based on the default BC settings in WACCM. The Modal Aerosol Model (MAM4) was employed to represent key aerosol processes. There are two parameters used to initialize fresh BC emissions: bc_{a4} and num_{a4}. The parameter bc_{a4} defines the number of molecules of fresh BC added to each grid cell per unit volume and time, whereas num_{a4} defines the corresponding number of aerosol particles emitted. The value of num_{a4} was verified to be consistent with the default aircraft BC emissions input to MAM4.

CESM2 is allowed to run two different aerosol models, the Community Aerosol and Radiation Model for Atmospheres (CARMA) and MAM4 (Toon et al., 1988; Bardeen et al., 2008, 2013; Yu et al., 2015; Liu et al., 2016; Tilmes et al., 2023). The main differences are the aerosol specifics. CARMA has two aerosol size description, while MAM4 microphysics describes four modes (Liu et al., 2016; Tilmes et al., 2023). Two of the four modes, primary carbon and accumulation mode, represent fresh and aged BC, respectively. The transition from primary carbon to the accumulation mode occurs through condensation and coagulation processes, during which carbon particles become coated with soluble species such as sulfates (Liu et al., 2016). The discussion from Tilmes et al. (2023) concluded that CARMA generally provides a more accurate representation of aerosol size distributions and removal processes compared to the modal MAM4 approach, but both models can reasonably reproduce stratospheric and tropospheric aerosol properties when appropriately configured and constrained by observations. However, CARMA has significantly higher computational costs compared to MAM4, which can be a limitation for long-term simulations. Therefore, this study uses MAM4 as the aerosol module to balance computational efficiency with the required level of detail.

2.2 Design of Experiments

This study simulates launch emissions from the Earth's surface up to ∼70 km. Three species of rocket emissions are considered in this study: BC, H_2O, and NO_x. The total emitted BC integrated over model layers corresponding to geometric altitudes of 11–70 km is set to 30 Gg yr^{-1} in every case. This fixed 11–70 km BC emission definition is used only to standardize the imposed source strength across experiments; diagnostic BC and H_2O burdens reported later are instead evaluated from the model-diagnosed tropopause to 4.87×10^{-2} hPa. This emission rate is hypothetical and similar to that used by Maloney et al. (2022), which has been shown to produce statistically significant climate response anomalies. This emission rate corresponds to approximately 1×10^4 medium-lift kerosene rocket launches per year, or roughly 30 times the current launch rate, neglecting differences in launch vehicles and propellant types. A control simulation was performed without rocket emissions for comparison with the emission cases. To investigate the launch latitudinal dependencies, six year-round emission simulations were conducted at launch latitudes of 55° S, 29° S, 0° N, 29° N, 55° N, and 70° N. For the sake of benchmarking against real-world launch sites, the 29° N launch case can be referred to Cape Canaveral Space Force Station. The equatorial launch case can be associated with the Guiana Space Centre. The 70° N case represents a generic high-latitude launch location, where such lati-

Table 1. Summary of the simulated launch cases and the control case. 29° N, 81° W corresponds to Cape Canaveral Space Force Station, and 0° N, 50° W corresponds to the Guiana Space Centre. *An additional BC-only case was performed at 29° N.

Launch Lat.	Launch Lon.	Year-Round	Boreal Summer-only	Boreal Winter-only
55° S	68° W	✓	✓	✓
29° S	154° E	✓		
0° N	50° W	✓	✓	✓
29° N	81° W	✓*	✓	✓
55° N	2° W	✓		
70° N	120° E	✓	✓	✓
Control case without rocket emissions				

tudes are beneficial for polar and sun-synchronous orbits. To examine the seasonal dependencies, additional simulations were performed for boreal summer-only and boreal winter-only launches at 55° S, 0° N, 29° N, and 70° N. The emission timing for the boreal summer-only cases was set to June-August, whereas that for the boreal winter-only cases was set to December-February. The seasonal emission rate was set to 10 Gg per month to maintain an annual total equivalent to the year-round case (30 Gg yr^{-1}). To assess the long-term role of BC emissions relative to NO_x and H_2O, a case considering only BC emissions was conducted. For each case, 20 years of simulations were performed from 2000 to 2020, and the final 15 years were analyzed to obtain quasi-steady-state results. A list of the simulation cases is provided in Table 1.

2.3 Launch Trajectory and Emission Indices

Since this study focuses on emissions from a medium-lift kerosene rocket, a representative Falcon 9 ascent profile to geostationary transfer orbit was reconstructed using publicly available launch telemetry records (nas, 2016). While this source may have limitations in terms of reliability, it is used solely to prescribe the vertical distribution of rocket emissions. The resulting trajectory was compared with a Falcon 9 maximum-payload trajectory generated using a convex optimization framework based on the methodology of Benedikter et al. (2019), showing good agreement within the region of interest (Earth's surface to 70 km). Propellant flow rates for each stage are assumed constant and are derived from stage propellant masses of 412,854 kg and 107,500 kg for the first and second stages, respectively (Garner, 2022), with burn times of 162 s and 397 s as reported in Benedikter et al. (2019). Based on the results presented by Garner (2022) and Benedikter et al. (2019); Benedikter (2022), the maximum-payload trajectories of launch vehicles from the Earth's surface to 70 km appear to be relatively similar and exhibit low sensitivity to mission type and launch vehicle configuration. Although Brown et al. (2024b) developed a comprehensive rocket emission inventory, this study derived deposited rocket emissions from representative launch trajectories using emission indices Eq. (1 to 3). This approach provides greater flexibility for future investigations of how launch vehicle designs and trajectories influence climate impacts. The following list summarizes the information required to implement these emission profiles as inputs to WACCM.

1. Emissions are applied as continuous volumetric fluxes within each selected model grid cell at every model timestep. The flux rate is calculated by dividing the total annual emissions by the emission duration, which corresponds to the full year for year-round cases and the three-month launch period for seasonal cases.

2. The vertical profile of emissions, derived from trajectory data, is distributed across the model's vertical layers using a geometric altitude grid from the Earth's surface up to 70 km.

3. Emissions are assigned to the only launch site grid cell because the trajectory data from the Earth's surface to 70 km indicate limited downrange distance. Consequently, the effects of downrange emissions are assumed to be negligible.

4. BC emissions are introduced as primary carbon (fresh BC) at release. Subsequent transitions from the primary mode to the accumulation mode are handled by MAM4 through condensation and coagulation processes, particularly as BC particles are transported to lower altitudes where soluble species are more abundant.

5. NO_x emissions are released as nitrogen dioxide (NO_2), consistent with the default aircraft NO_x emissions in CESM, while H_2O emissions are added as water vapor.

A first-order estimate of the BC emissions index was developed specifically for LOX/RP-1 engines (Simmons, 2000; Alexeenko et al., 2002; Plastinin et al., 2005; James et al., 2021)

$$EI_f(BC) = EI_p(BC) \max\left\{0.04,\ \min\left[1,\ 0.04e^{0.12(h-15)}\right]\right\}, \tag{1}$$

where the $EI_p(BC)$ is the primary emission index of BC, representing the mass of BC emitted per unit mass of propellant at the nozzle exit plane. This value is assumed to be 25 g kg^{-1}. In addition, h represents the emission altitude, expressed in km.

For LOX/RP-1 engines, all NO_x emissions are produced through reactions between the high-temperature exhaust plume and atmospheric nitrogen. Hence, the final emissions index for NO_x comes from the secondary emissions. The estimation was developed from previous studies (Gomberg and Stewart, 1976; Leone and Turns, 1994; James et al., 2021). It can be written as:

$$EI_f(NO_x) = 33e^{-\frac{0.26}{h}}. \tag{2}$$

The $EI_f(NO_x)$ is highest at sea level and decreases exponentially with altitude due to the lower abundance of ambient nitrogen in the thinner atmosphere.

In addition to the primary emission index of H_2O, it is assumed that hydrogen in the exhaust plume reacts with ambient oxygen, further increasing H_2O production

$$EI_f(H_2O) = EI_p(H_2O) + \frac{MW_{H_2O}}{MW_H} EI_p(H) + \frac{MW_{H_2O}}{MW_{H_2}} EI_p(H_2) + EI_p(OH), \tag{3}$$

where MW denotes the molecular weight and accounts for the contribution of oxygen from the surrounding air. For a medium-lift kerosene rocket, the $EI_f(H_2O)$ is set to 374 g kg^{-1} and is assumed to remain constant with altitude (James et al., 2021).

3 Results

Results were averaged over the final 15 years of each simulation to ensure a quasi-steady state, defined as the period during which the global BC burden remains within 10 % of its long-term asymptotic value. Each year was treated as an independent sample, and statistical significance was assessed by testing paired differences (case minus control, seasonal minus year-round, and year-round (BC-only) minus year-round) against zero using a Student's t-test. The lag-1 autocorrelation of the difference time series was used to estimate effective sample sizes and to adjust the degrees of freedom for computing p-values. The model-diagnosed tropopause was used to analyze responses above the tropopause. The upper boundary of the stratosphere is assumed to be approximately 7.30×10^{-1} hPa ($\sim$50 km), which is used to obtain stratospheric responses such as stratospheric temperature and cloud fraction anomalies, whereas the upper boundary used to define the BC, H_2O, and NO_x burdens is 4.87×10^{-2} hPa ($\sim$70 km).

The sections below provide detailed results on emission burdens and impacts on stratospheric temperature, general circulation, O_3, and ERF. In brief, BC burden varies with launch location and season, tending to be higher for low-latitude launches and more favorable in the Southern Hemisphere (SH). Launch latitude is the primary factor controlling both the BC mass-weighted mean latitude and altitude, while seasonal timing has a strong influence on the BC mass-weighted mean latitude for low-latitude launches. Both BC burden and BC mass-weighted mean latitude show a strong correlation with stratospheric temperature anomalies (Fig. 1a,b). Changes in stratospheric temperature also influence the general circulation, which can alter atmospheric temperatures at locations remote from the launch latitude. O_3 anomalies are associated with stratospheric temperature anomalies in the Northern Hemisphere (NH) and from 0° N to 60° S, where warmer temperatures accelerate photochemical reactions, enhancing O_3 depletion (Fig. 1d to e). In the south polar region, O_3 concentrations show a strong negative correlation with stratospheric cloud fraction anomalies, driven by altered winter South Pole temperatures that influence PSC-favorable conditions (Fig. 1f). These results support the hypothesis that variations in the location and seasonal timing of rocket launches lead to differences in the distribution and transport of BC in the atmosphere, resulting in distinct regional and global climate impacts. The 29° N BC-only comparison supports a dominant role of BC in the long term climate responses simulated here, although the attribution relative to co-emitted NO_x and H_2O remains incomplete.

3.1 Emission Burdens

3.1.1 BC Burdens

Across all scenarios, it takes no more than five years of continuous emissions for the system to reach a quasi-steady state, which is defined as the point at which system values are within 10 % of their long-term asymptotic behavior. Accordingly, this study focuses on the final 15 years of the simulated response. The time series of BC burden evolution for the 0° N cases are shown in Fig. 2a to c, illustrating the temporal emissions of boreal summer-only and boreal winter-only launches. The annual mean BC burdens in the atmosphere between the tropopause (as diagnosed by the model) and 4.87×10^{-2} hPa are presented in Fig. 3 and Table 2. The differences in steady-state BC burdens among the cases are linked to the efficiency of general circulation in transporting BC from the emission source. The BC burden tends to be higher when the circulation allows for broader spatial

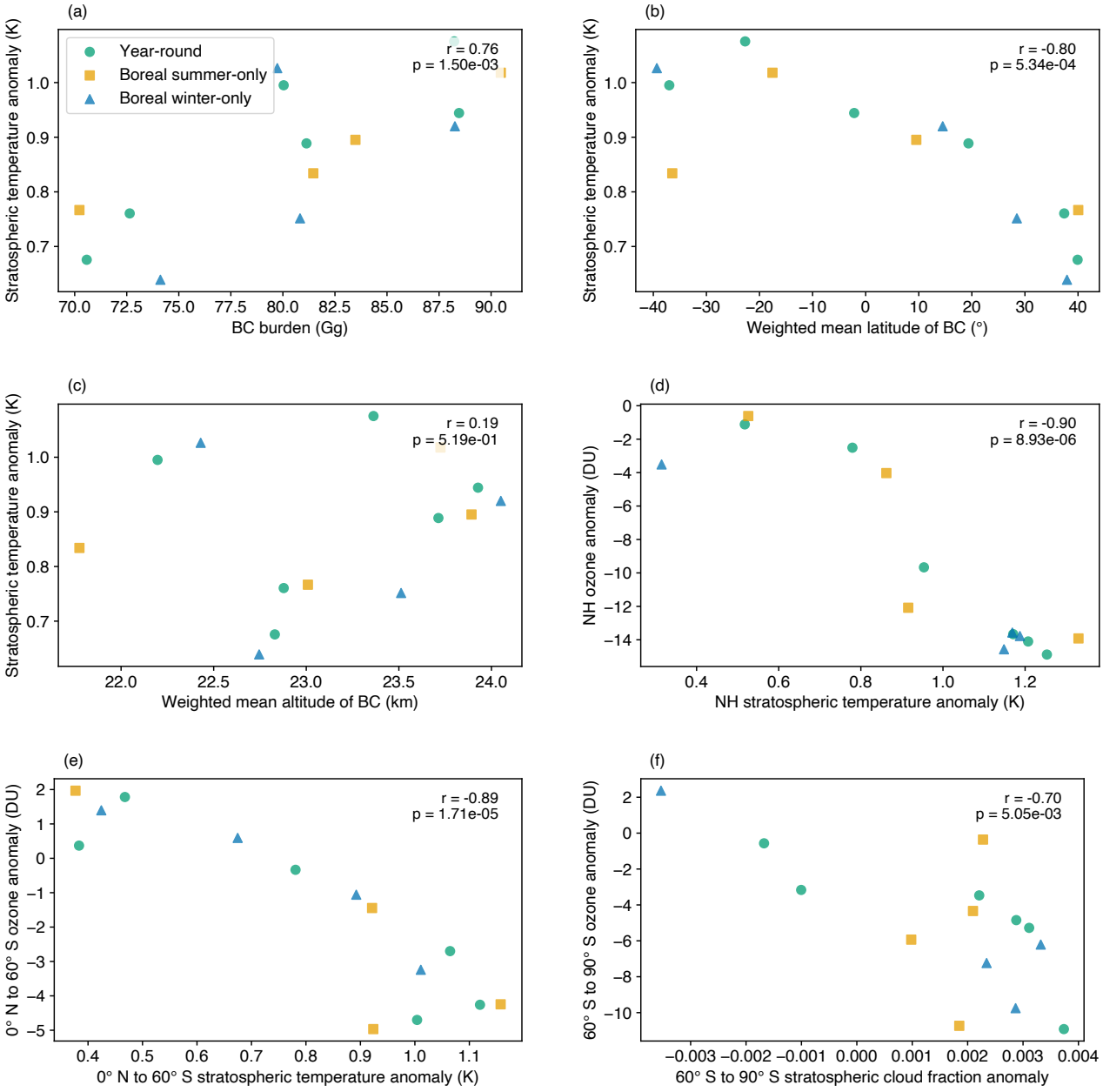

Figure 1. Case minus control correlations for each matrix: (a) Stratospheric temperature anomalies (K) versus BC burden (Gg). (b) versus BC mass-weighted mean latitude (°). (c) versus BC mass-weighted mean altitude (km). (d) Northern Hemisphere total O_3 column anomalies (DU) versus stratospheric temperature anomalies (K). (e) 0° N to 60° S total O_3 column versus stratospheric temperature anomalies (K). (f) 60° S to 90° S total O_3 column versus stratospheric cloud fraction anomalies.

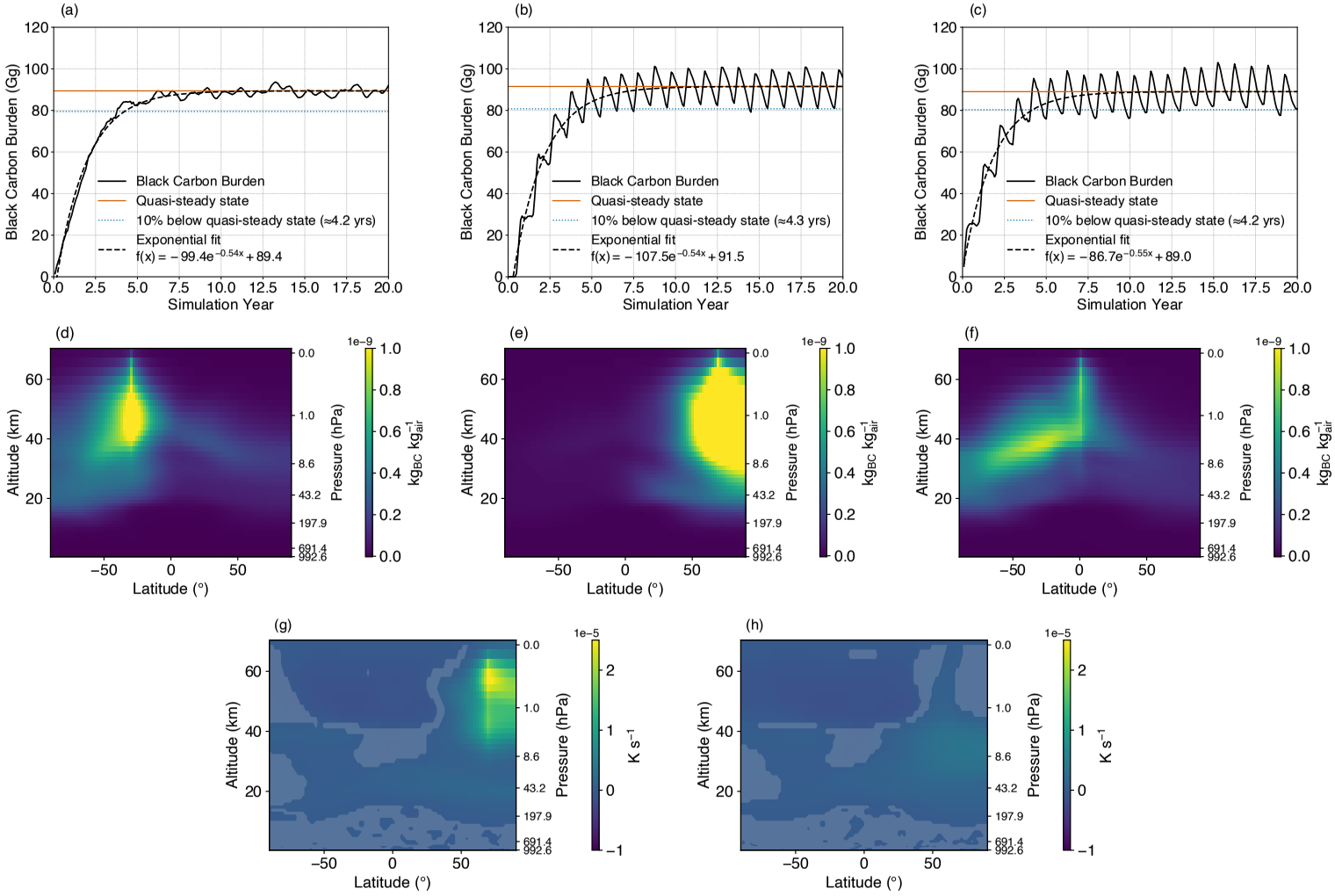

Figure 2. Case minus control time series of atmospheric BC burdens (Gg) between the tropopause and 4.87×10^{-2} hPa for 0° N launches for (a) year-round, (b) boreal summer-only, and (c) boreal winter-only cases. Steady-state BC distributions ($kg_{BC}\ kg_{air}^{-1}$) for (d) year-round 29° S launches, (e) year-round 70° N launches, and (f) boreal summer-only 0° N launches. Solar heating rate anomalies ($K\ s^{-1}$) for (g) 70° N boreal summer-only launches and (h) 70° N boreal winter-only launches. Regions with shading indicate areas where heating rate anomalies are not statistically significant relative to the control case.

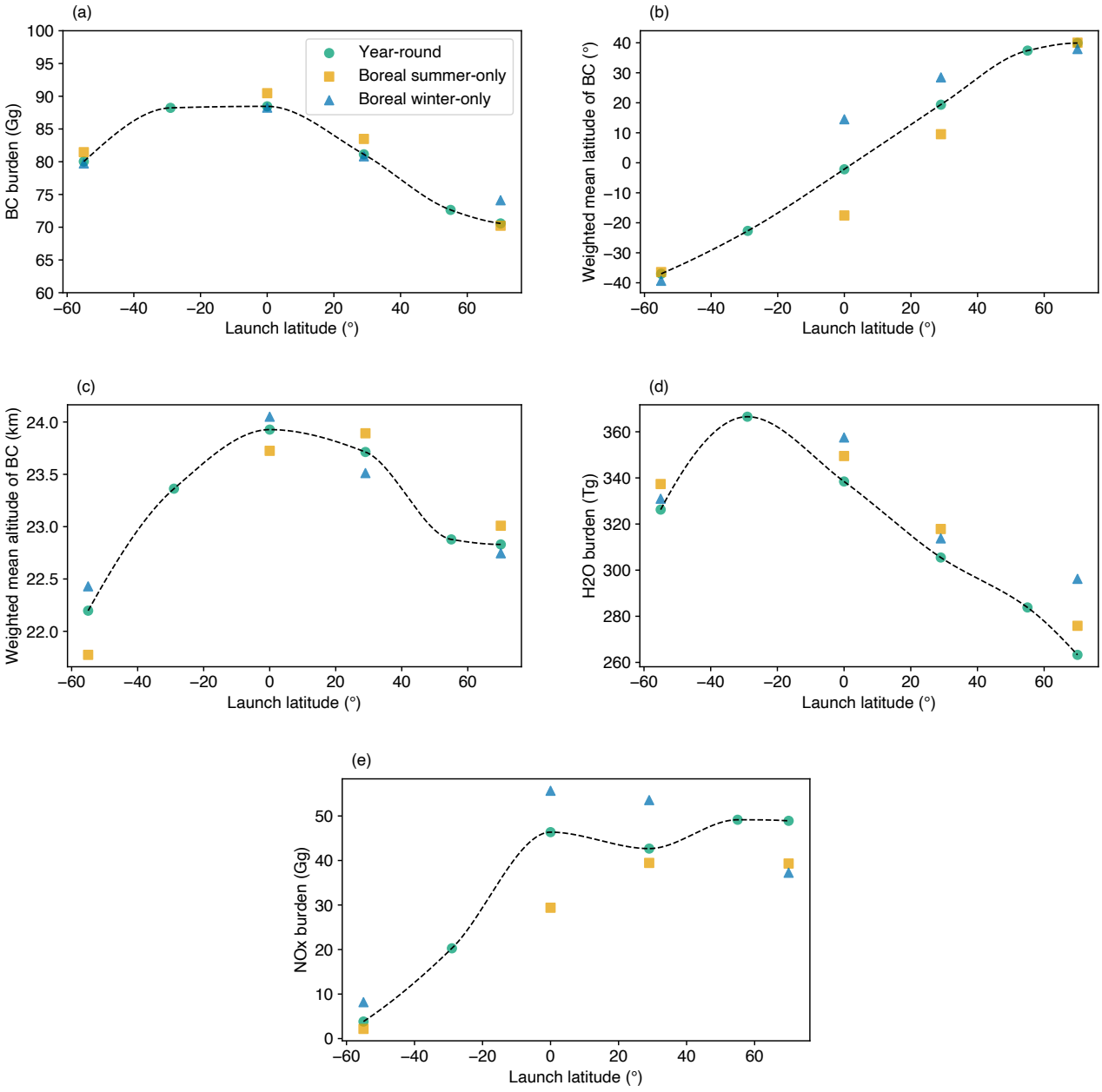

Figure 3. Case minus control differences in (a) atmospheric BC burdens (Gg) between the tropopause and 4.87×10^{-2} hPa at each launch latitude for year-round, boreal summer-only, and boreal winter-only cases. (b) BC mass-weighted mean latitude (°) from the Earth's surface to 4.87×10^{-2} hPa. (c) BC mass-weighted mean altitude (km) from the Earth's surface to 4.87×10^{-2} hPa. (d) atmospheric H_2O burdens (Tg) between the tropopause and 4.87×10^{-2} hPa. (e) NO_x ($NO + NO_2$) burdens (Gg) from the Earth's surface to 4.87×10^{-2} hPa. Piecewise Cubic Hermite Interpolating Polynomials (PCHIP) are used to connect the year-round responses across launch latitudes.

Table 2. Emission burdens averaged over the final 15 years of each climate model simulation (case minus control). BC and H_2O burdens are integrated from the atmosphere between the tropopause and 4.87×10^{-2} mb, while NO_x ($NO + NO_2$) burdens are calculated from the Earth's surface to 4.87×10^{-2} mb. The 29° N BC-only launch results are shown in parentheses.

		Launch Latitude (°)					
		55° S	29° S	0° N	29° N	55° N	70° N
BC Burdens (Gg)	Year-round	80.04	88.23	88.46	81.13 (81.45)	72.64	70.58
	Boreal summer-only	81.46	-	90.47	83.48	-	70.23
	Boreal winter-only	79.73	-	88.26	80.82	-	74.12
H_2O Burdens (Tg)	Year-round	326	367	338	305 (304)	284	263
	Boreal summer-only	337	-	349	318	-	276
	Boreal winter-only	331	-	358	314	-	296
NOx Burdens (Gg)	Year-round	3.83	20.28	46.37	42.67 (44.07)	49.15	48.91
	Boreal summer-only	2.18	-	29.39	39.46	-	39.32
	Boreal winter-only	8.18	-	55.66	53.57	-	37.25

transport, effectively distributing the aerosol over a wider region. Among the year-round cases, equatorial launches produce the highest BC burden (Fig. 3a and Table 2) at 88.46 Gg, nearly identical to the 29° S case at 88.23 Gg despite substantially different BC mass-weighted mean latitudes. This behavior suggests that transport into the SH favors longer BC residence times, potentially due to hemispheric differences in large-scale circulation and polar vortex structure. This interpretation is supported by comparisons between the 29° N and 29° S cases, as well as by the equatorial seasonal launch cases. The boreal summer-only case, with a BC mass-weighted mean latitude falls in the SH, produces higher BC burden than the year-round and boreal winter-only cases, both of which retain BC farther north. Figure 2d to f illustrates the steady-state BC distributions for year-round 29° S and 70° N launches, as well as boreal summer-only 0° N launches, highlighting the effects of launch latitude and season on BC distribution.

In terms of the BC mass-weighted mean altitude shown in Fig. 3c, the mean altitude increases as the launch latitude approaches the equator. This results from the weaker influence of the Brewer–Dobson circulation (BDC) downward transport combined with the stronger upward motion of warm tropical air, which allows BC to persist at higher altitudes. Launches near the pole that occur during the local winter undergo immediate downward transport, resulting in a lower mean BC altitude.

3.1.2 H_2O and NO_x Loadings

Based on the 30 Gg yr^{-1} BC emission rate, the corresponding annual H_2O emission rate is approximately 1 Tg yr^{-1}. Figure 3d and Table 2 show that the steady-state H_2O burden anomaly is substantially larger than the direct annual H_2O emission rate, corresponding to an increase of approximately 8–12 % relative to the baseline H_2O burden of 3,068 Tg between the diagnosed tropopause and 4.87×10^{-2} hPa. The 29° N BC-only case shows that even without direct rocket H_2O emissions, the H_2O burden remains close to that in the full-emission case, indicating that the simulated increase is largely indirect. A more plausible

explanation is that BC-induced warming modifies temperatures and transport near the tropical tropopause layer, allowing more H_2O to enter the stratosphere before being redistributed by the large-scale circulation. As stratospheric temperatures increase, more H_2O primarily enters the stratosphere through the tropical tropopause layer before being transported to other regions (Randel et al., 2004; Dessler et al., 2013; Nowack et al., 2023). The relationship between H_2O burden and stratospheric temperature anomalies is consistent with the corresponding trends shown in Fig. 3d and Fig. 4a. For NO_x (NO + NO_2), the burdens are calculated from the Earth's surface to 4.87×10^{-2} hPa, since most NO_x is released below 11 km, with only about 0.5 Gg of the approximately 33 Gg emitted annually occurring above it. As shown in Table 2, the 29° N BC-only case shows a diagnosed NO_x burden close to that in the full-emission case, indicating a primarily indirect contribution. The diagnosed NO_x burdens range from 2.18 Gg to 55.66 Gg, representing less than a 2 % increase relative to the baseline NO_x burden of 2,842 Gg. As presented in Fig. 3e, the diagnosed NO_x burden is lower for launches in the SH. Because the present analysis does not explicitly diagnose NO_y partitioning or denitrification, we do not attribute this hemispheric difference to a single mechanism. It likely reflects a combination of chemical partitioning, transport, and removal processes that vary with latitude and season.

3.2 Impacts on Stratospheric Temperature

Stratospheric BC absorbs incoming shortwave radiation from the Sun and re-emits energy at longer wavelengths, resulting in atmospheric heating. The effect of BC absorption of incoming solar shortwave radiation is illustrated in Fig. 2g to h. The influence of the BC altitude profile on the solar heating rate is evident. The 70° N boreal winter-only case shows weaker positive solar heating rate anomalies, which are primarily confined below 40 km and are caused by aged BC. Although aged BC has a higher absorption cross section due to a stronger lensing effect (Gao et al., 2008; Zhang et al., 2021), the solar heating rate is more sensitive to BC concentration at higher altitudes, likely because of the lower air density, and lower O_3 concentrations at high altitude allow more direct solar shortwave radiation to be absorbed by BC (Samset and Myhre, 2015).

3.2.1 Launch Latitudinal Dependency

As discussed in Sect. 3.1, varying the launch latitude alters both the vertical and latitudinal distribution of BC. Since BC induces warming, these distributional differences alter the resulting temperature anomaly profiles. Figure 5a shows that the warming pattern is spatially correlated with the launch latitude. Hemispheric asymmetry is observed, and launches at higher latitudes can intensify polar warming. This polar warming can strengthen the meridional wind in the mesosphere, resulting in altered temperatures at the opposite pole. This effect is evident in the 70° N launch case, even though the net cooling effect near the South Pole is not statistically significant. The effects of this are discussed in detail in Sect. 3.3. In terms of the role of BC in stratospheric temperature changes, the 29° N BC-only launches show a latitudinal temperature anomaly profile similar to that of the full-emissions 29° N case. At high southern latitudes, the 29° N BC-only case shows greater stratospheric warming. However, neither the global (Table 3) nor the latitudinal differences in stratospheric temperature anomalies between the 29° N BC-only and full-emissions 29° N cases are statistically significant (not shown).

Consistent with Table 3 and Fig. 4a, global mean stratospheric temperature anomalies generally increase as the launch latitude shifts away from the North Pole. The strongest warming occurs for the 29° S launch case, driven by South Pole and

Table 3. Results from the final 15 years of each climate model simulation. Year-round case results show differences between the cases and the control (case minus control), while seasonal case results show differences between the seasonal and year-round cases at the same launch latitude (seasonal minus year-round). The 29° N BC-only launch results show differences relative to the 29° N year-round case (year-round (BC-only) minus year-round). Bold values denote anomalies that are statistically significant ($p < 0.05$), relative to the control case for year-round results and to the year-round case for seasonal results, as determined using Student's t-test.

		Launch Latitude (°)					
		55° S	29° S	0° N	29° N, (29° N BC-only)	55° N	70° N
Stratospheric T	Year-round	**1.00 ± 0.10**	**1.08 ± 0.12**	**0.94 ± 0.12**	**0.89 ± 0.14**, (0.08 ± 0.13)	**0.76 ± 0.11**	**0.68 ± 0.12**
(K)	Boreal summer-only	**-0.16 ± 0.15**	-	0.07 ± 0.10	0.01 ± 0.15	-	0.09 ± 0.14
	Boreal winter-only	0.03 ± 0.19	-	-0.02 ± 0.15	-0.14 ± 0.15	-	-0.04 ± 0.12
O_3 Column	Year-round	-2.26 ± 2.26	**-3.22 ± 1.88**	**-6.54 ± 2.59**	**-7.61 ± 2.94**, (0.45 ± 3.04)	**-6.87 ± 1.50**	**-8.98 ± 2.32**
(DU)	Boreal summer-only	-0.74 ± 1.77	-	1.32 ± 1.98	0.48 ± 2.87	-	**2.78 ± 2.63**
	Boreal winter-only	-0.18 ± 2.66	-	-1.50 ± 2.91	-0.94 ± 3.08	-	1.51 ± 2.92
All-sky TOA ERF	Year-round	**0.42 ± 0.23**	**0.38 ± 0.18**	**0.35 ± 0.22**	**0.26 ± 0.20**, (-0.09 ± 0.21)	**0.18 ± 0.16**	**0.18 ± 0.15**
(W m^{-2})	Boreal summer-only	0.05 ± 0.22	-	0.05 ± 0.24	0.08 ± 0.16	-	0.12 ± 0.18
	Boreal winter-only	-0.03 ± 0.20	-	-0.16 ± 0.24	-0.16 ± 0.20	-	0.09 ± 0.20
Clear-sky TOA ERF	Year-round	0.10 ± 0.23	-0.08 ± 0.14	0.06 ± 0.20	-0.06 ± 0.22, (-0.10 ± 0.20)	-0.05 ± 0.22	-0.07 ± 0.19
(W m^{-2})	Boreal summer-only	0.04 ± 0.21	-	-0.00 ± 0.14	0.12 ± 0.15	-	0.10 ± 0.11
	Boreal winter-only	-0.06 ± 0.25	-	-0.14 ± 0.18	-0.11 ± 0.21	-	0.04 ± 0.14
All-sky TOA SW	Year-round	**1.09 ± 0.25**	**1.03 ± 0.17**	**0.82 ± 0.24**	**0.77 ± 0.20**, (-0.07 ± 0.23)	**0.57 ± 0.18**	**0.49 ± 0.20**
(W m^{-2})	Boreal summer-only	-0.07 ± 0.18	-	0.12 ± 0.22	0.03 ± 0.21	-	0.19 ± 0.29
	Boreal winter-only	-0.14 ± 0.22	-	-0.15 ± 0.23	-0.20 ± 0.27	-	0.16 ± 0.21
All-sky TOA LW	Year-round	**0.67 ± 0.21**	**0.65 ± 0.17**	**0.47 ± 0.23**	**0.51 ± 0.16**, (0.02 ± 0.13)	**0.39 ± 0.14**	**0.32 ± 0.16**
(W m^{-2})	Boreal summer-only	-0.12 ± 0.18	-	0.07 ± 0.28	-0.06 ± 0.16	-	0.07 ± 0.14
	Boreal winter-only	-0.11 ± 0.20	-	0.02 ± 0.23	-0.04 ± 0.16	-	0.06 ± 0.12
Clear-sky TOA SW	Year-round	**0.68 ± 0.14**	**0.47 ± 0.12**	**0.49 ± 0.16**	**0.39 ± 0.17**, (-0.07 ± 0.20)	**0.28 ± 0.18**	**0.22 ± 0.17**
(W m^{-2})	Boreal summer-only	-0.07 ± 0.14	-	0.04 ± 0.16	0.05 ± 0.18	-	0.15 ± 0.16
	Boreal winter-only	**-0.18 ± 0.14**	-	-0.13 ± 0.16	-0.15 ± 0.21	-	0.07 ± 0.15
Clear-sky TOA LW	Year-round	**0.58 ± 0.20**	**0.55 ± 0.15**	**0.43 ± 0.20**	**0.46 ± 0.14**, (0.03 ± 0.09)	**0.33 ± 0.14**	**0.29 ± 0.17**
(W m^{-2})	Boreal summer-only	-0.11 ± 0.17	-	0.04 ± 0.26	-0.06 ± 0.13	-	0.04 ± 0.15
	Boreal winter-only	-0.12 ± 0.18	-	0.01 ± 0.18	-0.03 ± 0.13	-	0.03 ± 0.10

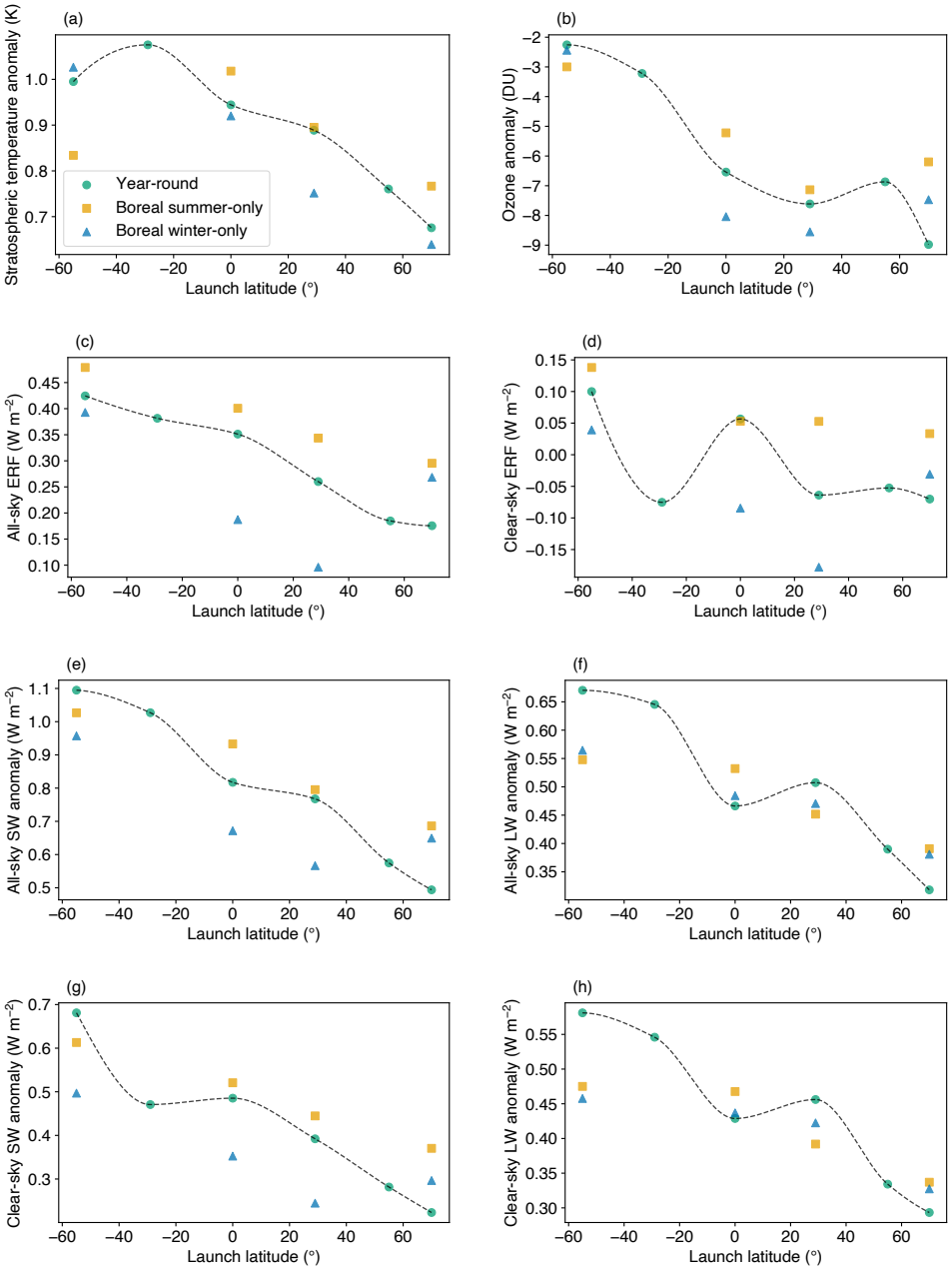

Figure 4. Case minus control differences in (a) stratospheric temperature anomalies (K) at each launch latitude for year-round, boreal summer-only, and boreal winter-only cases. (b) total O_3 column anomalies (DU). (c) all-sky ERF anomalies (Wm^{-2}) at TOA. (d) clear-sky ERF anomalies (Wm^{-2}) at TOA. (e) all-sky shortwave radiation anomalies (Wm^{-2}) at TOA. (f) all-sky longwave radiation anomalies (Wm^{-2}) at TOA. (g) clear-sky shortwave radiation anomalies (Wm^{-2}) at TOA. (h) clear-sky longwave radiation anomalies (Wm^{-2}) at TOA. PCHIP are used to connect the year-round responses across launch latitudes.

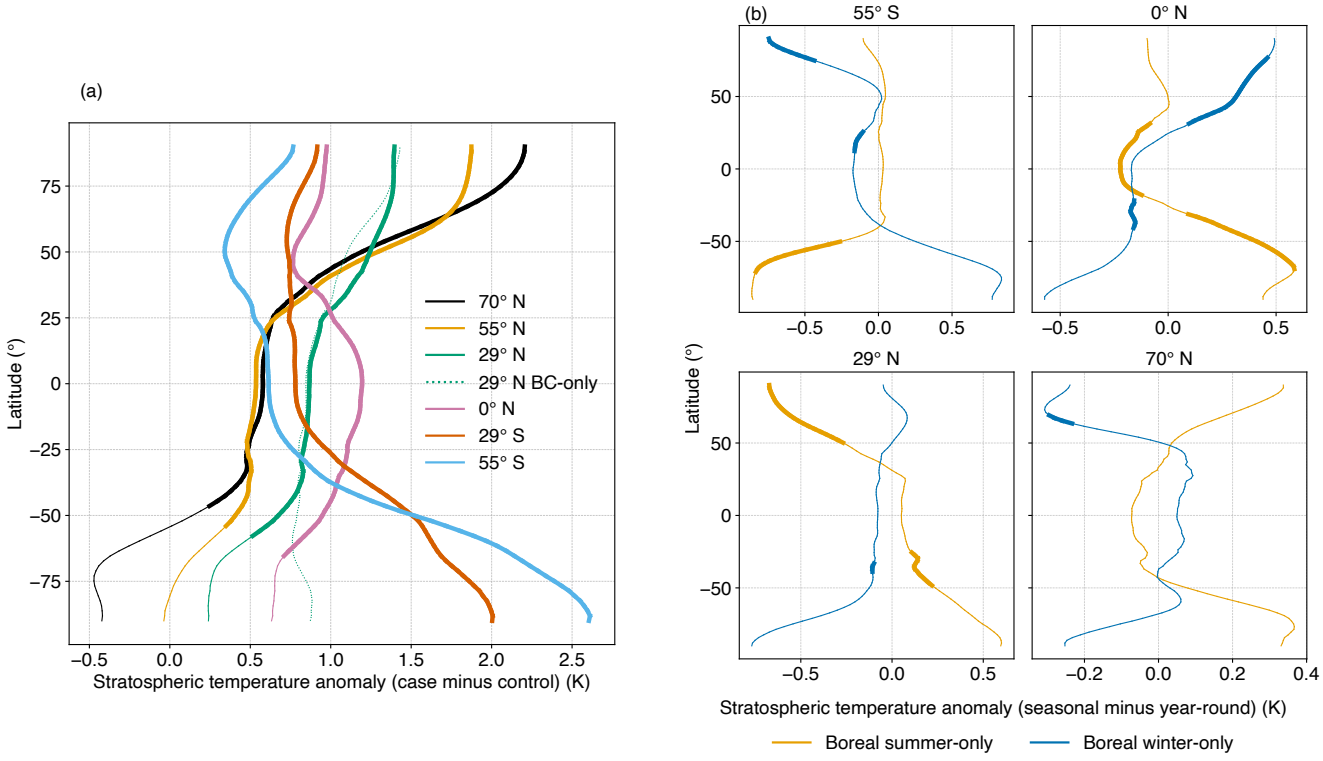

Figure 5. (a) Latitudinal stratospheric temperature anomalies (K) for each year-round launch latitude case (case minus control). (b) Latitudinal stratospheric temperature anomalies for boreal summer-only and boreal winter-only simulations (seasonal minus year-round). Results are shown for four launch latitudes (55° S, 0° N, 29° N, and 70° N). Thick lines indicate statistically significant values, whereas thin lines denote non-significant values compared to the control case. Statistical indicators for 29° N BC-only in Fig. a are omitted for clarity.

tropical warming combined with a relatively high stratospheric BC burden. The positive correlations between stratospheric temperature anomalies and BC burden, as well as with BC mass-weighted mean latitude, are shown in Fig. 1a,b.

3.2.2 Launch Seasonal Dependency

For comparison purposes, Fig. 5b shows the differences between the seasonal cases and the year-round case at the same launch latitude, along with the corresponding Student's t-test used to assess statistical significance. At 55° S launches, most statistically significant results indicate colder conditions relative to the year-round launches. Boreal summer-only launches result in colder conditions in the SH due to lower BC mass-weighted mean altitudes. Boreal winter-only launches induce stronger changes in the general circulation due to the higher BC mean altitude, thereby altering temperatures over the North Pole and leading to colder conditions. More details on changes in the general circulation are presented in Sect. 3.3. At equatorial launches, changes in stratospheric temperature are strongly correlated with BC transport, with higher BC content leading to warmer conditions in

that hemisphere. The same interpretation can be applied to the 29° N launches. At 70° N launches, boreal winter-only launches result in relatively colder conditions at high latitudes in the NH due to lower BC altitudes. For the global changes, only the boreal summer-only 55° S launches show statistically significantly less warming relative to the year-round case by 0.16 ± 0.15 (Table 3). Indeed, the global stratospheric temperature anomalies are strongly correlated with the BC mass-weighted mean latitude and altitude. The overall correlations are illustrated in Fig. 1b,c. Note that Fig. 1c does not show a statistically significant correlation because the effect of BC mass-weighted mean altitude is dominated by the mean BC latitude when launches occur farther from the poles.

3.3 Impacts on General Circulation

Rocket emissions can alter atmospheric temperatures, thereby inducing changes in atmospheric circulation. At the same time, changes in vertical dynamics can influence atmospheric temperatures through adiabatic warming and cooling processes (Holton and Hakim, 2013). Warming from BC forcing typically occurs near the summer pole, accompanied by an upward wind anomaly above the heated region. It is observed from the results that this upward motion turns meridional upon reaching the mesopause, heading toward the winter pole. Upon reaching the opposite pole at the mesopause, the flow diverges, generating both upward and downward wind anomalies and thereby altering the atmospheric temperature. Warming at the winter pole generally occurs in the upper stratosphere and mesosphere, whereas the middle and lower stratosphere experience cooling, likely due to temperature inversion and adiabatic compensation. The circulation and temperature anomalies exhibit characteristics similar to those observed during SSW events (Baldwin et al., 2021; Eswaraiah et al., 2022; Okui et al., 2025).

3.3.1 Launch Latitudinal Dependency

As shown in Fig. 6a to c, changes in the general circulation are stronger when launches occur at higher latitudes, specifically strengthening the meridional wind toward the winter pole. Indeed, southern launches appear to produce stronger anomalies than northern launches at the same latitude. At the South Pole, launches from the NH are likely to produce a stratospheric cooling signal during JJA. This effect is more evident and statistically significant for high-latitude NH launches (Fig. 6c), whereas launches from the SH produce year-round stratospheric warming due to persistent aerosol-induced heating. At the North Pole, launches from all latitudes are likely to produce cooling in the lower stratosphere and warming in the upper stratosphere during DJF, although the response is not statistically significant.

3.3.2 Launch Seasonal Dependency

The 70° N launches (Fig. 6c,d) are shown because they produce the most pronounced changes in the general circulation. The largest circulation changes occur during JJA, with the boreal summer-only launches producing the strongest anomalies. However, the year-round case appears to have the largest temperature changes around the South Pole, leading to the coldest stratospheric South Pole during JJA. This is likely because a southward wind anomaly develops as early as MAM, driven by continuous emissions that begin altering the temperature during that period. The anomaly is sufficiently strong to disrupt

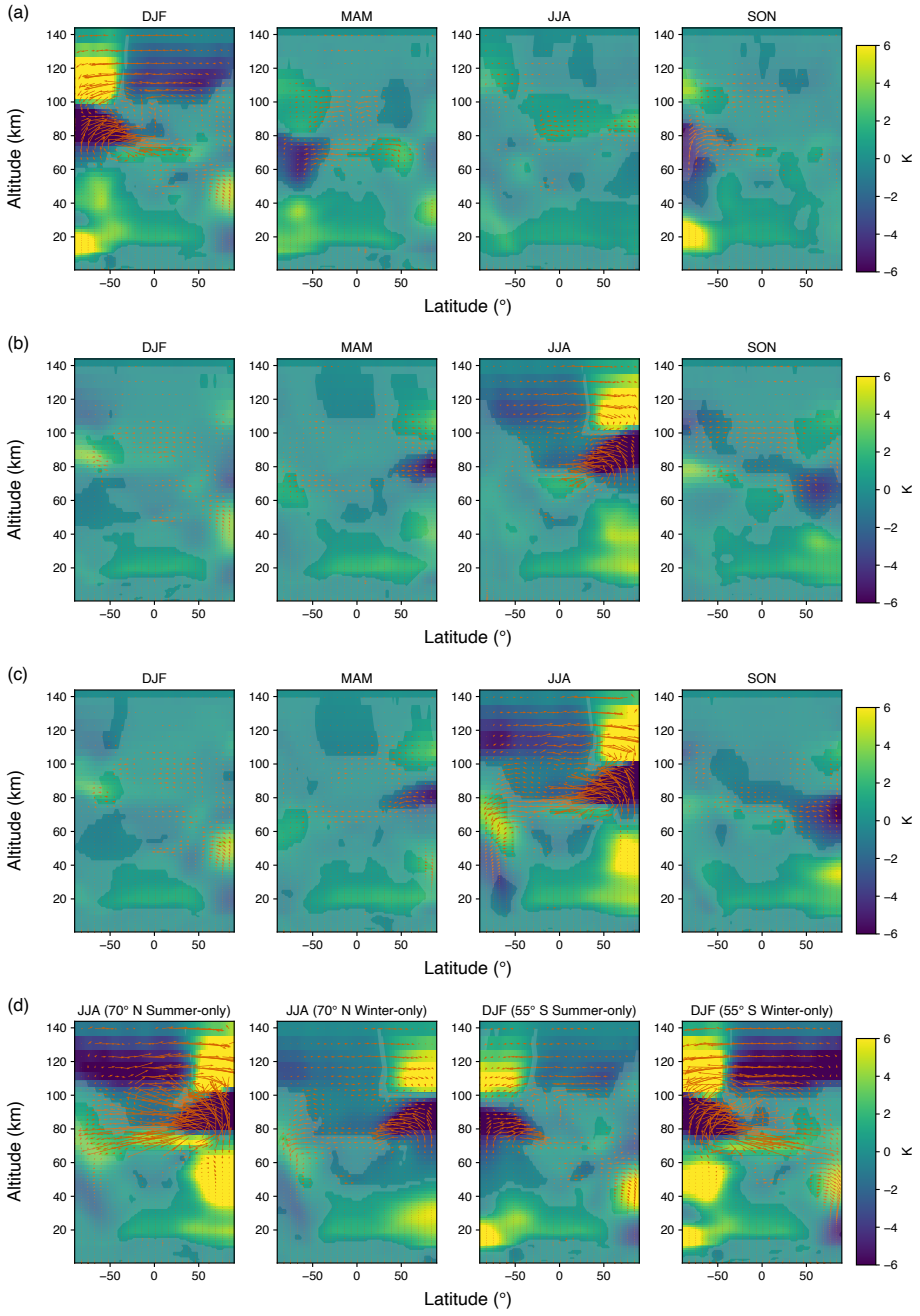

Figure 6. Temperature and wind anomalies for DJF, MAM, JJA, and SON (case minus control): (a) 55° S year-round launches, (b) 55° N year-round launches, (c) 70° N year-round launches, and (d) 70° N and 55° S seasonal launches, showing the hemispheric summer months at the respective launch locations. For visualization, the vertical wind component is scaled by a factor of 50 and the meridional wind component reduced by a factor of 2. Regions with shading indicate areas where the temperature anomalies are not statistically significant compared to the control case.

the South Pole temperatures during the presence of the polar vortex. Although the boreal summer-only launches seem to produce the strongest wind anomalies, they generate the weakest southward wind anomalies reaching the South Pole during JJA due to the mesospheric warming that extends into the tropics. This warming likely disrupts the uniform meridional wind anomaly. In contrast, despite the stronger tropical mesospheric warming, the 55° S boreal winter-only case (Fig. 6d) produces more pronounced stratospheric cooling over the North Pole during DJF. This inconsistent behavior may arise from a relatively weaker NH polar vortex, which allows greater stratospheric temperature alterations during NH winter.

3.4 Impacts on O_3

The observed O_3 changes in this study are most consistent with BC-induced stratospheric temperature and circulation changes. This interpretation is supported by the 29° N BC-only case (Table 3, Fig. 7), where the O_3 anomaly profile is very similar to that of the 29° N full-emissions case, except at high southern latitudes where the BC-only case shows slightly less O_3 loss. These differences are not statistically significant. Comparisons with previous work suggest that substantially larger H_2O and NO_x emissions than those considered here may be required to produce statistically significant global O_3 responses (Larson et al., 2017), consistent with the relatively minor role of H_2O and NO_x in our simulations.

In the NH and the nonpolar SH, warmer upper stratospheric temperatures accelerate photochemical reactions, leading to enhanced O_3 depletion. Near the South Pole, cooler stratospheric temperatures enhance ice-containing clouds under PSC-favorable conditions, consistent with processes that influence O_3 loss. As shown in Fig. 7b,c, the changes in south polar cloud fraction are accompanied by increases in ice condensate with negligible liquid condensate, indicating that the diagnosed clouds represent physically realized ice clouds rather than a cloud fraction increase driven solely by changes in relative humidity.

3.4.1 Launch Latitudinal Dependency

Figure 7a shows that total O_3 column losses are likely to be more pronounced in the NH because baseline O_3 concentrations are higher than in the SH. In the NH, launches closer to the North Pole cause stronger local O_3 depletion, while the sensitivity of O_3 loss to launch latitude increases as launch locations move closer to the equator. There is a strong correlation between NH O_3 loss and NH stratospheric temperature anomalies, as shown in Fig. 1d. Similar behavior is also observed between 0° N and 60° S, as shown in Fig. 1e. These correlations are consistent with photochemical processes enhanced under warmer stratospheric conditions. In the South Polar region, 70° N launches lead to the largest total O_3 column loss likely due to enhanced cooling near the South Pole during local winter (Fig. 6c), which promotes conditions favorable for ice-containing clouds consistent with PSC formation (Fig. 7b,c). This correlation is shown in Fig. 1f.

As shown in Fig. 4b and Table 3, the greatest global total O_3 column loss occurs in the 70° N case. O_3 depletion decreases as the launch latitude shifts toward the South Pole. Interestingly, launches from 55° N do not follow the trend. This is due to the effect of the 70° N launches, which uniquely cool the winter South Pole and lead to the greatest O_3 loss. As the launch latitude shifts toward the equator, this effect diminishes significantly, as shown in Fig. 7a. Comparing the 55° N and 29° N launches shows that total O_3 column anomalies in the NH are relatively insensitive to launch latitude, exhibiting nearly identical values.

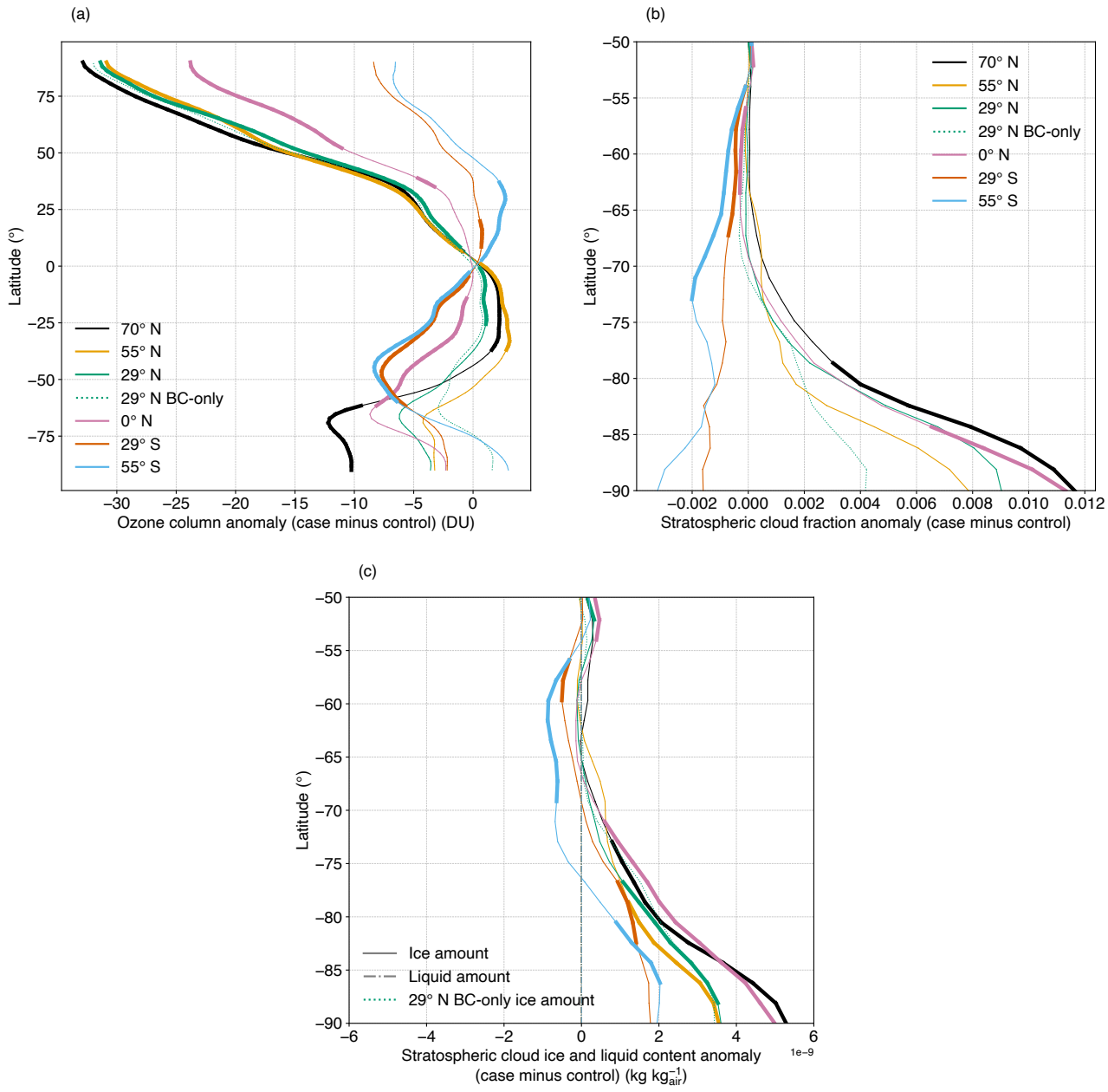

Figure 7. (a) Latitudinal total O_3 column anomalies for each year-round launch latitude case (case minus control). Negative values indicate a reduction in O_3 column content relative to the control. (b) Latitudinal stratospheric cloud fraction anomalies for each year-round launch latitude case. (c) Latitudinal stratospheric cloud ice and liquid content anomalies for each year-round launch latitude case. Thick lines indicate statistically significant values, while thin lines denote non-significant values compared to the control case. Statistical indicators for 29° N BC-only and ice content are omitted for clarity.

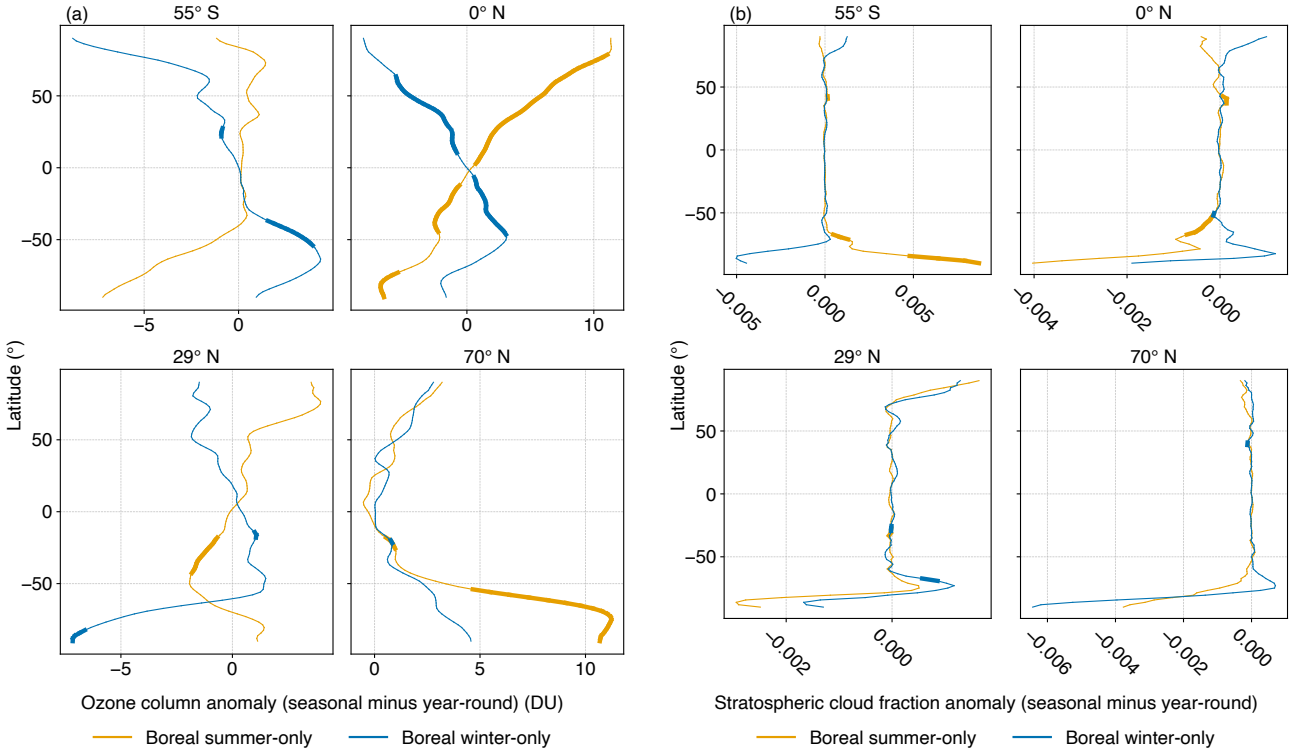

Figure 8. Results of boreal summer-only and boreal winter-only simulations compared to the year-round simulation for four launch latitudes (55° S, 0° N, 29° N, and 70° N) (seasonal minus year-round): (a) Latitudinal total O_3 column anomalies (DU). Negative values indicate a reduction in O_3 column content relative to the control. (b) Latitudinal stratospheric cloud fraction anomalies. Thick lines indicate statistically significant values, while thin lines denote non-significant values compared to the year-round case.

However, in the 29° N case, warmer conditions in the SH result in enhanced O_3 loss there, thereby having lower global O_3 levels than the 55° N case.

3.4.2 Launch Seasonal Dependency

As shown in Fig. 8a, the 55° S boreal winter-only case shows a statistically significant gain in total O_3 column in the SH, likely driven by regional warming which suppresses PSC-favorable conditions. However, the reduction in stratospheric cloud fraction at the South Pole itself is not statistically significant. Launches at 0° N exhibit total O_3 column anomaly profiles that are strongly correlated with BC distributions. For example, more BC resides in the SH in the boreal summer-only case, leading to greater O_3 loss there relative to the year-round case. The 29° N boreal winter-only case shows a decrease in total O_3 column at the South Pole, likely due to indications of colder conditions in the SH associated with disrupted general circulation, which further promotes PSC-favorable condition. All the seasonal launches at 70° N have more O_3 content relative to the year-

round case, likely due to a colder South Pole stratosphere during JJA in the year-round case, which promotes PSC-favorable conditions (as supported by Fig. 8b and discussed in Sect. 3.3).

For global O_3 change, only the 70° N boreal summer-only case shows a statistically significant difference relative to the year-round case, with a global O_3 gain of 2.78 ± 2.63 DU.

3.5 Changes in Radiative Forcings

The net shortwave radiation at the TOA is defined as the difference between incoming solar radiation and reflected solar radiation, while the net longwave radiation corresponds to the outgoing thermal emission from the Earth system. As BC absorbs shortwave radiation, both directly from the Sun and reflected by the Earth's atmosphere and surface, it warms the surrounding air. This atmospheric heating enhances thermal emission, increasing outgoing longwave radiation. The resulting changes in radiative fluxes create the ERF. In CESM, the radiation scheme first computes radiative fluxes under all-sky conditions, while clear-sky fluxes are subsequently diagnosed using the cloud fraction simulated by the model.

In the BC-only case, none of the radiative parameters are statistically significant relative to the full-emissions scenario as shown in Table 3. This suggests that, under the emission magnitudes considered in this study, the direct radiative contributions of co-emitted H_2O and NO_x are likely smaller than the BC-driven contribution. Consistent with prior studies (Ryan et al., 2022; Maloney et al., 2022), Larson et al. (2017) showed that at least 3×10^5 launches with H_2O and NO_x emissions are required to produce a statistically significant ERF, more than two orders of magnitude greater than the emissions considered in this study.

3.5.1 Launch Latitudinal Dependency

As shown in Fig. 4c to h, both the all-sky and clear-sky shortwave and longwave radiation anomalies are positive. The positive shortwave radiation anomalies indicate that BC absorbs reflected solar radiation, thereby retaining more shortwave energy within the Earth system. The magnitude of shortwave radiation anomalies increases as the launch location moves closer to the South Pole, potentially due to the influence of O_3 content. Larger drops in O_3 content from northern latitude launches enhance upwelling due to reduced atmospheric solar absorption. A similar trend is observed for longwave radiation anomalies, as the additional absorbed energy is re-emitted at longer wavelengths through thermal emission. While both shortwave and longwave clear-sky fluxes show statistically significant responses, they largely offset each other, resulting in a statistically insignificant clear-sky ERF. In contrast, the all-sky ERF remains significant, indicating that cloud radiative effects modulate the net radiative response.

3.5.2 Launch Seasonal Dependency

Only the boreal winter-only launches at 55° S produce a statistically significant decrease in clear-sky shortwave flux of 0.18 ± 0.14 W m^{-2} relative to the year-round launches (Table 3). For the other launch cases, the year-round configurations produce the most extreme anomalies in both all-sky and clear-sky longwave radiation, as well as in all-sky and clear-sky shortwave radiation for high-latitude launches. These indicate that continuous emissions may have a strong influence on the global radiation budget.

Future work is needed to better understand the processes driving these responses, including a detailed analysis of cloud-fraction changes across latitude and altitude and their contribution to radiative forcing.

4 Conclusions

This study used WACCM6 to quantify how the latitude and seasonal timing of rocket launches influence long-term atmospheric and climate responses. Emissions from a medium-lift kerosene launch vehicle were applied at an annual BC emission rate of 30 Gg yr^{-1}, integrated over geometric altitudes of approximately 11–70 km. We find that the launch latitude strongly impacts the spatial distribution of BC and associated climate responses. Southern latitude launches produce a greater steady-state global BC burden and stronger stratospheric warming than those from the north. However, O_3 depletion is more pronounced for northern launches, reflecting higher baseline northern hemisphere O_3 concentrations. The total O_3 column is primarily regulated by the stratospheric temperature, with an anticorrelation between O_3 concentrations and stratospheric cloud fraction anomalies observed in the South Polar region. Both all-sky and clear-sky shortwave and longwave radiation anomalies are larger for southern hemisphere launches, a pattern that also extends to the all-sky ERF. In contrast, the clear-sky ERF shows no statistically significant changes in any case.

When comparing the year-round cases of 29° N, representative of Cape Canaveral Space Force Station, and 29° S launches, the 29° S launch results in greater stratospheric warming by 0.19 ± 0.16 K. However, it results in a smaller global total O_3 column loss by 4.39 ± 3.30 DU. The final changes in all-sky and clear-sky ERF are not statistically significant.

Seasonal timing also modulates BC transport and climate responses. For low-latitude launches during boreal summer, a greater fraction of BC is transported into the SH, leading to enhanced regional and global stratospheric warming but causing less O_3 depletion. At high-latitude launches, the launch season primarily controls the steady-state BC altitude, with local winter launches confining BC to lower altitudes and therefore producing less warming. However, O_3 variations resulting from launch seasonality at high latitudes do not exhibit a consistent trend, likely owing to the complex interplay between dynamical transport, temperature variability, and chemical feedback mechanisms. Across all seasonal cases, statistically significant changes are limited to three cases relative to the year-round case: the global total O_3 column in the 70° N boreal summer-only case (+2.78 ± 2.63 DU), the global stratospheric temperature in the 55° S boreal summer-only case (-0.16 ± 0.15 K), and the clear-sky shortwave flux in the 55° S boreal winter-only case (-0.18 ± 0.14 W m^{-2}). Additional statistically significant differences appear in the latitudinal profiles of stratospheric temperature and O_3 anomalies, primarily near the poles.

When focusing on the 29° N (Cape Canaveral) launches, the boreal summer-only case shows less warming near the stratospheric North Pole, up to ≈ 0.7 K, while the boreal winter-only case shows more total O_3 column loss near the South Pole up to ≈ 7 DU.

Results confirm the hypothesis that both launch latitude and seasonal timing impact the steady-state distribution and transport of BC, thereby shaping distinct long-term regional and global climate impacts. Several limitations should be noted. The emissions rate used in this study is hypothetical to ensure detectable climate responses, but is consistent with prior studies. Only a single launch vehicle and propellant type were considered, and only a limited set of emission species (BC, H_2O, and NO_x)

were included. An identical emission vertical profile was applied to all cases. Emissions were applied as continuous, time-averaged fluxes, which do not capture the short-term variability of individual launches. The WACCM6 simulations used fixed year-2000 SSTs with middle atmosphere chemistry, and BC microphysics were represented using MAM4. These assumptions should be considered when interpreting the quantitative results.

This study extends our understanding of how different emission locations and timings from rocket launches affect the long-term climate. By linking launch characteristics to climate responses, the results provide a metric that can support environmentally informed decision-making for future applications, such as the development and optimization of spaceport infrastructure. Future work will apply these insights to identify environmentally optimal launch sites and timing strategies for different space mission types, accounting for trade-offs between launch cost and climate impact. Furthermore, understanding how different emission vertical profiles and magnitudes influence the climate will be beneficial for launch vehicle design and trajectory optimization aimed at minimizing both launch costs and environmental impacts.

Code and data availability. The model simulations performed using WACCM6/CESM2. Software for this research is available in these in-text data citation references (Gettelman et al., 2019; Danabasoglu et al., 2020). The datasets and the software code used for performing data analysis and producing the manuscript's figures in the study are available at the University of Michigan Deep Blue Repositories via https://doi.org/10.7302/txz8-fm65 (Wongprapinkul et al., 2026) with a Creative Commons Public Domain license (CC0 1.0).

Author contributions. N.W., G.C., and O.J. conceptualized the study. N.W. developed the methodology, performed the validation, conducted the formal analysis and investigation, prepared the original draft, and produced the visualizations. N.W., G.C., and O.J. reviewed and edited the manuscript. G.C. and O.J. provided supervision.

Competing interests. All authors declare no financial or non-financial competing interests.

Acknowledgements. N. Wongprapinkul is supported by a Royal Thai Government Scholarship, funded by the Geo-Informatics and Space Technology Development Agency, Thailand, and this work was also supported by an exploratory allocation through the NCAR Derecho system. We gratefully acknowledge the NCAR HPC University Allocations Program for providing access to high-performance computing resources essential to this research.

References

Timing is critical as launch windows approach, https://www.esa.int/Enabling_Support/Space_Transportation/Timing_is_critical_as_launch_windows_approach, accessed: 2026-05-05, 2002.

Falcon 9 velocity/altitude values from webcast, https://forum.nasaspaceflight.com/index.php?topic=40983.0, accessed: 2025-04-29, 2016.

Alexeenko, A. A., Gimelshein, N. E., Levin, D., Collins, R., Rao, R., Candler, G., Gimelshein, S., Hong, J., and Schilling, T.: Modeling of flow and radiation in the Atlas plume, Journal of Thermophysics and heat Transfer, 16, 50–57, https://doi.org/10.2514/2.6651, 2002.

Baldwin, M. P., Ayarzagüena, B., Birner, T., Butchart, N., Butler, A. H., Charlton-Perez, A. J., Domeisen, D. I., Garfinkel, C. I., Garny, H., Gerber, E. P., et al.: Sudden stratospheric warmings, Reviews of Geophysics, 59, e2020RG000 708, https://doi.org/10.1029/2020RG000708, 2021.

Bardeen, C., Toon, O., Jensen, E., Marsh, D., and Harvey, V.: Numerical simulations of the three-dimensional distribution of meteoric dust in the mesosphere and upper stratosphere, Journal of Geophysical Research: Atmospheres, 113, https://doi.org/10.1029/2007JD009515, 2008.

Bardeen, C., Gettelman, A., Jensen, E., Heymsfield, A., Conley, A., Delanoë, J., Deng, M., and Toon, O.: Improved cirrus simulations in a general circulation model using CARMA sectional microphysics, Journal of Geophysical Research: Atmospheres, 118, 11–679, https://doi.org/10.1002/2013JD020193, 2013.

Benedikter, B.: Convex optimization of launch vehicle ascent trajectories, Ph.D. thesis, Università degli Studi di Roma" La Sapienza", https://doi.org/10.13140/RG.2.2.17244.87689, 2022.

Benedikter, B., Zavoli, A., Colasurdo, G., et al.: A convex approach to rocket ascent trajectory optimization, in: 8th European Conference for Aeronautics and Space Sciences (EUCASS), pp. 1–15, https://doi.org/10.13009/EUCASS2019-430, 2019.

Brown, T. F., Bannister, M. T., and Revell, L. E.: Envisioning a sustainable future for space launches: a review of current research and policy, Journal of the Royal Society of New Zealand, 54, 273–289, https://doi.org/10.1080/03036758.2022.2152467, 2024a.

Brown, T. F., Bannister, M. T., Revell, L. E., Sukhodolov, T., and Rozanov, E.: Worldwide rocket launch emissions 2019: an inventory for use in global models, Earth and Space Science, 11, e2024EA003 668, https://doi.org/10.1029/2024EA003668, 2024b.

Charlesworth, E., Plöger, F., Birner, T., Baikhadzhaev, R., Abalos, M., Abraham, N. L., Akiyoshi, H., Bekki, S., Dennison, F., Jöckel, P., et al.: Stratospheric water vapor affecting atmospheric circulation, Nature Communications, 14, 3925, https://doi.org/10.1038/s41467-023-39559-2, 2023.

Crutzen, P. J.: The influence of nitrogen oxides on the atmospheric ozone content, QJR Meteorol. Soc, 96, 320–325, https://doi.org/10.1002/qj.49709640815, 1970.

Dallas, J., Raval, S., Gaitan, J. A., Saydam, S., and Dempster, A.: The environmental impact of emissions from space launches: A comprehensive review, Journal of Cleaner Production, 255, 120 209, https://doi.org/10.1016/j.jclepro.2020.120209, 2020.

Danabasoglu, G., Lamarque, J.-F., Bacmeister, J., Bailey, D., DuVivier, A., Edwards, J., Emmons, L., Fasullo, J., Garcia, R., Gettelman, A., et al.: The community earth system model version 2 (CESM2), Journal of Advances in Modeling Earth Systems, 12, e2019MS001 916, https://doi.org/10.1029/2019MS001916, 2020.

Dessler, A. E., Schoeberl, M. R., Wang, T., Davis, S. M., and Rosenlof, K. H.: Stratospheric water vapor feedback, Proceedings of the National Academy of Sciences, 110, 18 087–18 091, https://doi.org/10.1073/pnas.1310344110, 2013.

Eswaraiah, S., Seo, K.-H., Kumar, K. N., Ratnam, M. V., Koval, A. V., Jeong, J.-Y., Mengist, C. K., Lee, Y.-S., Greer, K., Hwang, J.-Y., et al.: Anthropogenic Influence on the Antarctic Mesospheric Cooling Observed during the Southern Hemisphere Minor Sudden Stratospheric Warming, Atmosphere, 13, 1475, https://doi.org/10.3390/atmos13091475, 2022.

Gao, R., Hall, S., Swartz, W., Schwarz, J., Spackman, J., Watts, L., Fahey, D., Aikin, K., Shetter, R., and Bui, T.: Calculations of solar shortwave heating rates due to black carbon and ozone absorption using in situ measurements, Journal of Geophysical Research: Atmospheres, 113, https://doi.org/10.1029/2007JD009358, 2008.

Garner, R. J.: Modelling launch vehicle emissions in an evolving space sector, Ph.D. thesis, University of Strathclyde, https://doi.org/10.48730/hp51-s325, 2022.

Gettelman, A., Mills, M., Kinnison, D., Garcia, R., Smith, A., Marsh, D., Tilmes, S., Vitt, F., Bardeen, C., McInerny, J., et al.: The whole atmosphere community climate model version 6 (WACCM6), Journal of Geophysical Research: Atmospheres, 124, 12 380–12 403, https://doi.org/10.1029/2019JD030943, 2019.

Gomberg, R. I. and Stewart, R. B.: A computer simulation of the afterburning processes occurring within solid rocket motor plumes in the troposphere, Tech. rep., NASA Langley Research Center Hampton, VA, United States, https://ntrs.nasa.gov/citations/19770008588, 1976.

Holton, J. R. and Hakim, G. J.: An introduction to dynamic meteorology, vol. 88, Academic press, 2013.

James, M. M., Lympany, S. V., Salton, A. R., Calton, M. F., Miake-Lye, R. C., and Wayson, R. L.: Commercial Space Vehicle Emissions Modeling, Tech. rep., National Academies of Sciences, Engineering, and Medicine, Washington, DC, https://doi.org/10.17226/26142, 2021.

Jones, K. L., Dhopade, P., and DeMarchi, L.: Spaceportopia: A Primer For Successful Launch Site Planning, https://researchspace.auckland.ac.nz/items/3d6befb6-e901-405a-b6ed-7f34ac38ef97, accessed: 2026-05-05, 2025.

Kirk-Davidoff, D. B., Hintsa, E. J., Anderson, J. G., and Keith, D. W.: The effect of climate change on ozone depletion through changes in stratospheric water vapour, Nature, 402, 399–401, https://doi.org/10.1038/46521, 1999.

Larson, E. J., Portmann, R. W., Rosenlof, K. H., Fahey, D. W., Daniel, J. S., and Ross, M. N.: Global atmospheric response to emissions from a proposed reusable space launch system, Earth's Future, 5, 37–48, https://doi.org/10.1002/2016EF000399, 2017.

Leone, D. and Turns, S.: Active chlorine and nitric oxide formation from chemical rocket plume afterburning, in: 32nd Aerospace Sciences Meeting and Exhibit, p. 788, https://doi.org/10.2514/6.1994-788, 1994.

Liu, X., Ma, P.-L., Wang, H., Tilmes, S., Singh, B., Easter, R., Ghan, S., and Rasch, P.: Description and evaluation of a new four-mode version of the Modal Aerosol Module (MAM4) within version 5.3 of the Community Atmosphere Model, Geoscientific Model Development, 9, 505–522, https://doi.org/10.5194/gmd-9-505-2016, 2016.

Maloney, C. M., Portmann, R. W., Ross, M. N., and Rosenlof, K. H.: The climate and ozone impacts of black carbon emissions from global rocket launches, Journal of Geophysical Research: Atmospheres, 127, e2021JD036 373, https://doi.org/10.1029/2021JD036373, 2022.

Myhre, G., Shindell, D., Bréon, F.-M., Collins, W., Fuglestvedt, J., Huang, J., Koch, D., Lamarque, J.-F., Lee, D., Mendoza, B., Nakajima, T., Robock, A., Stephens, G., Takemura, T., and Zhang, H.: Anthropogenic and Natural Radiative Forcing, Cambridge University Press, pp. 659–740, https://doi.org/10.1017/CBO9781107415324.018, 2014.

Nowack, P., Ceppi, P., Davis, S. M., Chiodo, G., Ball, W., Diallo, M. A., Hassler, B., Jia, Y., Keeble, J., and Joshi, M.: Response of stratospheric water vapour to warming constrained by satellite observations, Nature Geoscience, 16, 577–583, https://doi.org/10.1038/s41561-023-01183-6, 2023.

Okui, H., Sato, K., and Watanabe, S.: The Mechanism of Interhemispheric Coupling Revealed by a Gravity Wave-Permitting General Circulation Model, Journal of Geophysical Research: Atmospheres, 130, e2025JD043 763, https://doi.org/10.1029/2025JD043763, 2025.

Plastinin, Y., Karabadzhak, G., Khmelinin, B., Baula, G., and Rodionov, A.: Investigation of soot density in the LOX/kerosene engine booster exhaust of Atlas II and Atlas III from remote measurements of radiation intensity, in: 43rd AIAA Aerospace Sciences Meeting and Exhibit, p. 769, https://doi.org/10.2514/6.2005-769, 2005.

Randel, W. J., Wu, F., Oltmans, S. J., Rosenlof, K., and Nedoluha, G. E.: Interannual Changes of Stratospheric Water Vapor and Correlations with Tropical Tropopause Temperatures, Journal of the Atmospheric Sciences, 61, 2133 – 2148, https://doi.org/10.1175/1520-0469(2004)061<2133:ICOSWV>2.0.CO;2, 2004.

Ravishankara, A. R., Daniel, J. S., and Portmann, R. W.: Nitrous Oxide: The Dominant Ozone-Depleting Substance Emitted in the 21st Century, Science, 326, 123–125, https://doi.org/10.1126/science.1176985, 2009.

Revell, L. E., Bannister, M. T., Brown, T. F., Sukhodolov, T., Vattioni, S., Dykema, J., Frame, D. J., Cater, J., Chiodo, G., and Rozanov, E.: Near-future rocket launches could slow ozone recovery, npj Climate and Atmospheric Science, 8, 212, https://doi.org/10.1038/s41612-025-01098-6, 2025.

Rosenlof, K. H.: Changes in water vapor and aerosols and their relation to stratospheric ozone, Comptes Rendus. Géoscience, 350, 376–383, https://doi.org/10.1016/j.crte.2018.06.014, 2018.

Ross, M., Mills, M., and Toohey, D.: Potential climate impact of black carbon emitted by rockets, Geophysical Research Letters, 37, https://doi.org/10.1029/2010GL044548, 2010.

Ross, M. N.: Comparative Analysis of Climate Forcing and Ozone Depletion Caused by Emissions from Two Different Suborbital Launch Systems, in: ASCEND 2020, p. 4056, https://doi.org/10.2514/6.2020-4056, 2020.

Ross, M. N. and Sheaffer, P. M.: Radiative forcing caused by rocket engine emissions, Earth's Future, 2, 177–196, https://doi.org/10.1002/2013EF000160, 2014.

Ryan, R. G., Marais, E. A., Balhatchet, C. J., and Eastham, S. D.: Impact of rocket launch and space debris air pollutant emissions on stratospheric ozone and global climate, Earth's Future, 10, e2021EF002 612, https://doi.org/10.1029/2021EF002612, 2022.

Samset, B. H. and Myhre, G.: Climate response to externally mixed black carbon as a function of altitude, Journal of Geophysical Research: Atmospheres, 120, 2913–2927, https://doi.org/10.1002/2014JD022849, 2015.

Simmons, F.: Rocket exhaust plume phenomenology, American Institute of Aeronautics and Astronautics, Inc., https://doi.org/10.2514/4.989087, 2000.

Tian, W., Chipperfield, M. P., and Lü, D.: Impact of increasing stratospheric water vapor on ozone depletion and temperature change, Advances in Atmospheric Sciences, 26, 423–437, https://doi.org/10.1007/s00376-009-0423-3, 2009.

Tilmes, S., Mills, M. J., Zhu, Y., Bardeen, C. G., Vitt, F., Yu, P., Fillmore, D., Liu, X., Toon, B., and Deshler, T.: Description and performance of a sectional aerosol microphysical model in the Community Earth System Model (CESM2), Geoscientific Model Development, 16, 6087–6125, https://doi.org/10.5194/gmd-16-6087-2023, 2023.

Toon, O. B., Turco, R., Westphal, D., Malone, R., and Liu, M.: A multidimensional model for aerosols: Description of computational analogs, Journal of Atmospheric Sciences, 45, 2123–2144, https://doi.org/10.1175/1520-0469(1988)045<2123:AMMFAD>2.0.CO;2, 1988.

Tsigaridis, K., Field, R., Bauer, S. E., Ross, M. N., Maloney, C., Schmidt, G. A., and Rosenlof, K. H.: Composition and Climate Impacts of increasing launches to Low Earth Orbit, in: AIAA SCITECH 2024 Forum, p. 2168, https://doi.org/10.2514/6.2024-2168, 2024.

Vogel, B., Feck, T., and Grooß, J.-U.: Impact of stratospheric water vapor enhancements caused by CH4 and H2O increase on polar ozone loss, Journal of Geophysical Research: Atmospheres, 116, https://doi.org/10.1029/2010JD014234, 2011.

Wongprapinkul, N., Cinar, G., and Jia-Richards, O.: Dependence of Atmospheric and Climate Impacts on Launch Latitude and Seasonal Variation in Rocket Emissions [Data set], https://doi.org/10.7302/txz8-fm65, 2026.

Yu, P., Toon, O. B., Bardeen, C. G., Mills, M. J., Fan, T., English, J. M., and Neely, R. R.: Evaluations of tropospheric aerosol properties simulated by the community earth system model with a sectional aerosol microphysics scheme, Journal of Advances in Modeling Earth Systems, 7, 865–914, https://doi.org/10.1002/2014MS000421, 2015.

Yu, P., Toon, O. B., Bardeen, C. G., Zhu, Y., Rosenlof, K. H., Portmann, R. W., Thornberry, T. D., Gao, R.-S., Davis, S. M., Wolf, E. T., de Gouw, J., Peterson, D. A., Fromm, M. D., and Robock, A.: Black carbon lofts wildfire smoke high into the stratosphere to form a persistent plume, Science, 365, 587–590, https://doi.org/10.1126/science.aax1748, 2019.

Yu, P., Davis, S. M., Toon, O. B., Portmann, R. W., Bardeen, C. G., Barnes, J. E., Telg, H., Maloney, C., and Rosenlof, K. H.: Persistent Stratospheric Warming Due to 2019–2020 Australian Wildfire Smoke, Geophysical Research Letters, 48, e2021GL092 609, https://doi.org/10.1029/2021GL092609, e2021GL092609 2021GL092609, 2021.

Zhang, X., Mao, M., Chen, H., Yin, Y., and Tang, S.: Lensing effect of black carbon with brown coatings: Dominant microphysics and parameterization, Journal of Geophysical Research: Atmospheres, 126, e2020JD033 549, https://doi.org/10.1029/2020JD033549, 2021.